Signal-domain optimization metrics for MPRAGE RF pulse design in parallel transmission at 7 tesla

V. Gras, A. Vignaud, F. Mauconduit, M. Luong, A. Amadon, D. Le Bihan, N. Boulant

▶ **To cite this version:**

V. Gras, A. Vignaud, F. Mauconduit, M. Luong, A. Amadon, et al.. Signal-domain optimization metrics for MPRAGE RF pulse design in parallel transmission at 7 tesla. Magnetic Resonance in Medicine, 2016, 76 (5), pp.1431-1442. 10.1002/mrm.26043 . hal-02103495

HAL Id: hal-02103495
https://hal.science/hal-02103495

Submitted on 18 Apr 2019

HAL is a multi-disciplinary open access archive for the deposit and dissemination of scientific research documents, whether they are published or not. The documents may come from teaching and research institutions in France or abroad, or from public or private research centers.

L'archive ouverte pluridisciplinaire **HAL**, est destinée au dépôt et à la diffusion de documents scientifiques de niveau recherche, publiés ou non, émanant des établissements d'enseignement et de recherche français ou étrangers, des laboratoires publics ou privés.

Signal-domain optimization metrics for MPRAGE RF pulse design in parallel transmission at 7 Tesla

V. Gras[1], A. Vignaud[1], F. Mauconduit[2], M. Luong[3], A. Amadon[1], D. Le Bihan[1], and N. Boulant [*1]

[1]Neurospin, CEA/DSV/I2BM, CEA Saclay, Gif-sur-Yvette, France

[2]Siemens Healthcare, Saint-Denis, France

[3]CEA/DSM/IRFU, CEA Saclay, Gif-sur-Yvette, France

Word count: 5100

7 Figures

2 Tables

[*]Corresponding author – Address: Neurospin, CEA/DSV/I2BM, CEA Saclay, 91191 Gif-sur-Yvette cedex, France – email: nicolas.boulant@cea.fr – tel.: (+33)169087682

Abstract

Purpose: Standard radiofrequency (RF) pulse design strategies focus on minimizing the deviation of the flip angle (FA) from a target value, which is sufficient but not necessary for signal homogeneity. An alternative approach, based directly on the signal, here is proposed for the MPRAGE sequence, and is developed in the parallel transmission (pTx) framework with the use of the k_T-points parametrization.

Methods: The FA-homogenizing and the proposed methods were investigated numerically under explicit power and specific absorption rate (SAR) constraints and tested experimentally in vivo on a 7 T pTx system enabling real time local SAR monitoring. RF pulse performance was assessed by a careful analysis of the signal and contrast between white and gray matter.

Results: Despite a slight reduction of the FA uniformity, an improved signal and contrast homogeneity with a significant reduction of the SAR was achieved with the proposed metric in comparison with standard pulse designs.

Conclusion: The proposed joint optimization of the inversion and excitation pulses enables significant reduction of the SAR in the MPRAGE sequence while preserving image quality. The work reported thus unveils a possible direction to increase the potential of ultra-high field MRI and pTx.

Keywords: Ultra high field; Parallel transmission; RF pulse design; SAR; MPRAGE; k_T-points; B1 inhomogeneity mitigation.

Introduction

The magnetization prepared rapid gradient echo sequence (1), referred to as MPRAGE, is extensively used in the neuro-imaging community and in routine neuroradiological examinations to provide high-resolution anatomical images of the brain with an excellent contrast between white matter (WM) and gray matter (GM) (2, 3). To acquire in vivo brain images at higher resolution, it is natural to explore the possibilities offered by ultra-high magnetic field (UHF) as the signal-to-noise ratio (SNR) capability increases at least linearly with field strength. Unfortunately, UHF imaging over an extended field-of-view (FOV) often poses problems due to the increasing transmit profile (B_1^+) inhomogeneities as the wavelength of the radio-frequency (RF) field becomes smaller (4). An inhomogeneous excitation indeed results in regional losses of contrast, or signal voids. To mitigate this effect, the use of short three-dimensional tailored RF pulses, known as k_T-points, and parallel transmission (pTx)(5) has been proposed for 3D acquisitions (6). This technique can be used to achieve an homogeneous excitation in the fast low-angle shot (FLASH) readout but also to achieve excellent inversion profiles for the magnetization preparation. Interestingly, k_T-points inversion pulses are also less SAR intensive than adiabatic inversion pulses (7) and require lower peak power levels for the same inversion quality (8).

For the design of k_T-points, minimizing the normalized root mean square error (NRMSE) deviation from the uniform target FA (9) appears as the natural choice for the objective function as it provides a robust RF pulse design method, disregarding specific features of the sequence for which it is intended. However, as it will be shown later, by virtue of the non-linear dependence of the MPRAGE signal with the FA (2), guaranteeing a low NRMSE for the FA is not absolutely necessary to yield a good signal uniformity. A metric that would take this non-linear behavior into account would probably improve pulse performance and possibly also reduce SAR, a critical aspect at UHF. To this end, we propose an alternative pulse design technique in which the deviation from the nominal MR signal and contrast are involved while SAR constraints are enforced explicitly (10, 11). We first demonstrate in simulation at 7 T that this new approach allows improving image quality as measured by the homogeneity of the signal or contrast between WM and GM, while decreasing SAR.

Finally, we compare in vivo at 7 T a standard RF pulse design based on the minimization of the NRMSE of the FA with the proposed optimization technique and verify experimentally the benefit of this new approach.

Theory

Design of k_T-points pulses under explicit power and SAR constraints

The design of non-selective k_T-points pulses with homogeneous target FA α_{t} consists in solving the magnitude least-squares (MLS) problem (10):

$$\begin{aligned} &\min \left\| |\mathcal{A}(\mathbf{x})| - \alpha_{\mathrm{t}} \right\|_2 , \\ &\mathbf{x} \in \mathbb{C}^{N_c N_{k_T}} . \end{aligned} \qquad [1]$$

In Eq. 1, N_c and N_{k_T} denote the number of channels and k_T-points respectively, $\mathbf{x} \in \mathbb{C}^{N_c N_{k_T}}$ is the complex vector composed of the RF coefficients applied to the different channels and normalized to the highest voltage $V_{\max}$ applicable at the coil input. Finally, $\mathcal{A} : \mathbb{C}^{N_c N_{k_T}} \rightarrow \mathbb{C}^{N_v}$ represents the tip-angle operator, i.e., the operator that returns the complex FA (12) produced by the excitation $\mathbf{x}$ in each of the N_v voxels subjected to the optimization. The latter operator is a function of the RF coefficients, the RF sub-pulse and blip durations (assumed to be identical for each k_T-point) T_s and T_b, the k_T locations in k-space $\mathbf{k}_1$, $\cdots$, $\mathbf{k}_{N_{k_T}}$ (rad/m), the voxel positions $\mathbf{r}_1$, $\cdots$, $\mathbf{r}_m$, the RF field maps created by each transmit channel $B_{1,[n]}(\mathbf{r}_m)$ $(1 \leq n \leq N_c)$ and the static field inhomogeneity $\Delta B_0(\mathbf{r}_m)$. In the small tip-angle regime, this operator is linear and thus can be written in matrix form (13).

To take into account hardware and SAR limits, the optimization problem is solved under explicit SAR and power constraints. The latter (peak and average power) are:

$$x_k \, x_k^{\star} \leq 1, \; 1 \leq k \leq N_c N_{k_T} . \qquad [2]$$

and

$$c_{\mathrm{P},n}(\mathbf{x}) \underset{\text{def.}}{=} \frac{V_{\max}^2}{Z_0} \, x_{[n]}^{\dagger} x_{[n]} \leq \frac{P_{\max}}{D}, \; 1 \leq n \leq N_c , \qquad [3]$$

where $Z_0 = 50\ \Omega$ is the input impedance of each transmit channel, $x_{[n]} = (x_{n+(j-1)N_c})_{1\leq j\leq N_{k_T}}$ (RF coefficients for the n^{th} channel) and where D denotes the duty cycle of the pulse. The SAR constraints are global (one inequality) and local ($N_Q \gg 1$ inequalities) and ensure that the power absorbed by the body does not exceed global safety, $\text{SAR}_{\text{G,max}}$, and local safety limits, $\text{SAR}_{10\,\text{g,max}}$, calculated over 10 g contiguous tissue. These constraints can be written as (10, 11):

$$c_{\mathbf{Q}_\text{G}}(\mathbf{x}) \underset{\text{def.}}{=} \frac{V_{\text{max}}^2}{Z_0} \sum_{1\leq j\leq N_{k_T}} \mathbf{x}(j)^\dagger\, \mathbf{Q}_\text{G}\, \mathbf{x}(j) \leq \frac{\text{SAR}_{\text{G,max}}}{D} \qquad [4]$$

and:

$$1 \leq k \leq N_Q,\ c_{\mathbf{Q}_k}(\mathbf{x}) \underset{\text{def.}}{=} \frac{V_{\text{max}}^2}{Z_0} \sum_{1\leq j\leq N_{k_T}} \mathbf{x}(j)^\dagger\, \mathbf{Q}_k\, \mathbf{x}(j) \leq \frac{\text{SAR}_{10\,\text{g,max}}}{D}\,, \qquad [5]$$

where $\mathbf{x}(j) = (x_{n+(j-1)N_c})_{1\leq n\leq N_c}$ (RF coefficients of the j^{th} k_T-point) and where $\mathbf{Q}_\text{G}$ and $\mathbf{Q}_1, \cdots, \mathbf{Q}_{N_Q} \in \mathbb{C}^{N_c\times N_c}$ represent the normalized SAR-matrices (kg^{-1}) for the estimation of the global and local RF power deposition (14, 15). To handle the many local constraints, one often makes use of the virtual observation point (VOP) compression model to greatly decrease the number of constraints (14, 16), so that here N_Q refers to the size of the VOP model, and is typically ≤ 200 for brain imaging.

In Eq. 1, the FA deviation is measured with respect to the L_2 norm. This metric is particularly convenient when the term that is evaluated (here $\mathcal{A}(\mathbf{x})$) is linear in $\mathbf{x}$ because it reduces then to the minimization of a quadratic function. However, it is not the case in the present problem where only the magnitude of the FA is considered and where $\mathcal{A}$ is a linear operator only in the limit of small FAs. Now, since $\big\||\mathcal{A}(\mathbf{x})| - \alpha_\text{t}\big\|_p$ approaches the maximum FA deviation over all evaluated voxels as $p \to \infty$, it can be of interest to substitute in Eq. 1 the L_2 norm by the L_p norm with $p > 2$ to penalize more large FA deviations. Below, the choice of the norm coefficient p thus is left free.

Joint design of the inversion and excitation pulses in MPRAGE

The implementation of the MPRAGE sequence with a pTx system requires the design of inversion and small FA (SFA) pulses. For the SFA pulse, where α_t is typically $< 10°$, the small FA approximation can be used. For the inversion pulse however, this approximation

breaks down and a full Bloch integration is necessary. Since both pulses are applied in the same sequence, the designs of these pulses are interconnected through the power and SAR constraints. A possible approach to address this problem is a joint optimization where the objective function is defined as the sum of the objective functions for the inversion and the SFA pulses:

$$
\begin{aligned}
&\min \left(\left\| \frac{|\mathcal{A}_{\mathrm{Inv}}(\mathbf{x})|}{\alpha_{\mathrm{t,Inv}}} - 1 \right\|_p^p + \left\| \frac{|\mathbf{A}_{\mathrm{SFA}}\mathbf{y}|}{\alpha_{\mathrm{t,SFA}}} - 1 \right\|_p^p \right)^{1/p} \underset{\text{def.}}{=} U_\alpha(\mathbf{x},\mathbf{y})\,, \\
&\mathbf{x} \in \mathbb{C}^{N_c N_{k_T}^{\mathrm{Inv}}},\ \mathbf{y} \in \mathbb{C}^{N_c N_{k_T}^{\mathrm{SFA}}}\,, \\
&\text{s. t.} \begin{cases}
D_{\mathrm{Inv}}\, c_{\mathbf{Q}_\mathrm{G}}(\mathbf{x}) + D_{\mathrm{SFA}}\, c_{\mathbf{Q}_\mathrm{G}}(\mathbf{y}) \le \mathrm{SAR}_{\mathrm{G,max}}\,, \\
\mathrm{SAR}_{10\,\mathrm{g},k}(\mathbf{x},\mathbf{y}) = D_{\mathrm{Inv}}\, c_{\mathbf{Q}_k}(\mathbf{x}) + D_{\mathrm{SFA}}\, c_{\mathbf{Q}_k}(\mathbf{y}) \le \mathrm{SAR}_{10\,\mathrm{g,max}},\ 1 \le k \le N_Q\,, \\
x_k\, x_k^\star \le 1,\ y_l\, y_l^\star \le 1,\ 1 \le k \le N_c \times N_{k_T}^{\mathrm{SFA}} \text{ and } 1 \le l \le N_c \times N_{k_T}^{\mathrm{Inv}}\,, \\
D_{\mathrm{Inv}}\, c_{\mathrm{P},n}(\mathbf{x}) + D_{\mathrm{SFA}}\, c_{\mathrm{P},n}(\mathbf{y}) \le P_{\max},\ 1 \le n \le N_c\,,
\end{cases}
\end{aligned}
\qquad [6]
$$

where $\mathbf{x}$ and $\mathbf{y}$ denote the coefficients of the inversion and the SFA pulses respectively while D_{Inv} and D_{SFA} represent their duty cycles. Equation 6 expresses the FA domain optimization problem.

Joint design targeting homogeneous MPRAGE signal and contrast

The MPRAGE signal for the central echo of the FLASH module can be expressed as a function of T_1, α_{Inv}, α_{SFA}, TR, TI, the echo spacing (ES) and the echo train length (ETL) (2). Let $\hat{s}(\mathrm{T}_1)$ denote the nominal MPRAGE signal, i.e. the signal that would be obtained if the inversion and the SFA pulse were perfect. Instead of measuring the deviation from the nominal angles α_{Inv} and α_{SFA}, it is possible, for assessing the overall pulse performance, to calculate instead the distance between the actual and the nominal signals, $s(\mathrm{T}_1)$ and $\hat{s}(\mathrm{T}_1)$, over a T_1 interval of interest I:

$$
f_s = \left(\frac{\int_I |s(\mathrm{T}_1) - \hat{s}(\mathrm{T}_1)|^p \, d\mathrm{T}_1}{\int_I \hat{s}(\mathrm{T}_1)^p \, d\mathrm{T}_1} \right)^{1/p}\,. \qquad [7]
$$

With brain imaging, the interval I may be chosen to encompass the T_1 values of WM ($\mathrm{T}_{1\mathrm{WM}}$) and GM ($\mathrm{T}_{1\mathrm{GM}}$). By construction, f_s vanishes for $s = \hat{s}$ in the interval I. This measure of signal deviation, f_s, is referred below as the signal fidelity.

Likewise a complementary criterion for evaluating pulse performance lies on the MPRAGE contrast:

$$c_s(\mathrm{T}_1, \mathrm{T}_1{}') = \frac{s(\mathrm{T}_1) - s(\mathrm{T}_1{}')}{s(\mathrm{T}_1) + s(\mathrm{T}_1{}')} \,. \qquad [8]$$

It is referred as the contrast fidelity f_c and is defined as the distance between the actual (c_s) and nominal contrast ($c_{\hat{s}}$):

$$f_c = \left(\frac{\int_{I\times I} |c_s(\mathrm{T}_1, \mathrm{T}_1{}') - c_{\hat{s}}(\mathrm{T}_1, \mathrm{T}_1{}')|^p \, d\mathrm{T}_1 d\mathrm{T}_1{}'}{\int_{I\times I} c_{\hat{s}}(\mathrm{T}_1, \mathrm{T}_1{}')^p \, d\mathrm{T}_1 d\mathrm{T}_1{}'} \right)^{1/p} . \qquad [9]$$

By construction, f_c vanishes if $s/\hat{s}$ is constant over I. In Eqs. 7 and 9, all T_1 values have implicitly the same contribution in the fidelity measure. Now, given that the distribution of T_1 in brain tissue is not uniform but rather bimodal, a more realistic definition of the fidelity would be to incorporate the probability density function for T_1 and to integrate from 0 to $+\infty$. However, to stay general and for simplicity, the latter refinement is not yet included.

In Fig. 1, the FA deviation (i.e. the objective function in Eq. 6), the signal fidelity and the contrast fidelity are mapped as a function of α_{Inv} and α_{SFA} for $p = 2$ and for $I = [\mathrm{T}_{1\mathrm{WM}} - 200\mathrm{ms}, \mathrm{T}_{1\mathrm{GM}} + 200\mathrm{ms}]$, assuming $\mathrm{T}_{1\mathrm{WM}}/\mathrm{T}_{1\mathrm{GM}} = 1.3/2$ s, i.e., typical T_1 values at 7 T (17). It appears that all metrics are minimized for $\alpha_{\mathrm{Inv}}/\alpha_{\mathrm{SFA}} = 180°/9°$, which are indeed the nominal FA values. But interestingly, Fig. 1.b shows that if $\alpha_{\mathrm{SFA}} < 9°$, then the optimal choice for α_{Inv} to minimize f_s is different than 180°. This criterion is therefore fundamentally different from the FA deviation criterion which does not introduce any dependence between the inversion and the SFA pulses. In a similar manner, the contrast fidelity (Fig. 1.c) appears to be conserved in a valley in the $(\alpha_{\mathrm{Inv}}, \alpha_{\mathrm{SFA}})$ space but differs from the one of the signal fidelity. Thus, combining both the signal and contrast fidelity, e.g. by taking $(f_s^2 + f_c^2)^{1/2}$ (Fig. 1.d), allows driving the desired inter-play between both RF pulses while penalizing large excursions of α_{SFA} or α_{Inv}.

A combination of both metrics can be used to define the following class of objective functions :

$$U_{f,\lambda}(\mathbf{x}, \mathbf{y}) = \left(\|F_{s,\mathbf{J}}(\mathbf{x}, \mathbf{y})\|_p^p + \lambda \, \|F_{c,\mathbf{J}}(\mathbf{x}, \mathbf{y})\|_p^p \right)^{1/p} , \qquad [10]$$

where $\lambda \geq 0$ is a scalar parameter that sets the relative importance of the signal and contrast terms, where the $N_v \times 1$ vectors $F_{s,\mathbf{J}}(\mathbf{x}, \mathbf{y})$ and $F_{c,\mathbf{J}}(\mathbf{x}, \mathbf{y})$ are the estimated signal fidelity and

contrast fidelity maps and where $\mathbf{J}$ is a set of T_1 values distributed in I so as to approximate the integrals in Eqs. (7) and (9). These vectors are defined as:

$$F_{s,\mathbf{J}}(\mathbf{x},\mathbf{y}) = \frac{\|\mathbf{S_J}(\mathbf{x},\mathbf{y}) - \hat{\mathbf{S}}_\mathbf{J}\|_p}{\|\hat{\mathbf{S}}_\mathbf{J}\|_p} \quad [11]$$

and:

$$F_{c,\mathbf{J}}(\mathbf{x},\mathbf{y}) = \frac{\|c_{\mathbf{S_J}}(\mathbf{x},\mathbf{y}) - c_{\hat{\mathbf{S}}_\mathbf{J}}\|_p}{\|c_{\hat{\mathbf{S}}_\mathbf{J}}\|_p}\,, \quad [12]$$

where $\mathbf{S_J}(\mathbf{x},\mathbf{y})$, $\hat{\mathbf{S}}_\mathbf{J}$, $c_{\mathbf{S_J}}(\mathbf{x},\mathbf{y})$ and $c_{\hat{\mathbf{S}}_\mathbf{J}}$ are the discrete versions of s, $\hat{s}$, c_s and $c_{\hat{s}}$ respectively.

The aim is now to verify that the *signal domain* optimization, expressed as $U_{f,\lambda}$, improves pulse performance.

Methods

Pulse design performance simulations

In order to compare the objective functions $U_{f,\lambda}$ and U_α, we propose to simulate the L-curves of the respective optimization problems with respect to the peak local SAR constraint, which was recognized as the factor that mostly constraints the RF pulse optimization. For the performance metric, we propose to evaluate i) the RMS of the signal and contrast fidelity maps $f_{s/c,\mathrm{RMS}} =< f_{s/c}^2 >^{1/2}$ (obtained by numerical integration of Eqs. (7) and (9)); ii) the normalized standard deviation of the WM ($\mathbf{J} = \mathrm{T_{1WM}}$) and GM ($\mathbf{J} = \mathrm{T_{1GM}}$) signals:

$$\sigma_{\mathrm{WM,GM}} = \frac{\mathrm{Var}(\mathbf{S_J})^{1/2}}{\hat{\mathbf{S}}_\mathbf{J}}\,, \quad [13]$$

and iii) the standard deviation of the contrast between WM and GM (WM-GM contrast), where the respective signals are scaled with the proton density (PD) for WM ($\rho_{\mathrm{WM}} \simeq 0.7$) and GM ($\rho_{\mathrm{GM}} \simeq 0.8$) (18):

$$\sigma_{c^{(\rho)}} = \frac{\mathrm{Var}(c^{(\rho)})^{1/2}}{\hat{c}^{(\rho)}}\,, \quad [14]$$

where $c^{(\rho)}$ and $\hat{c}^{(\rho)}$ are defined as:

$$c^{(\rho)} = \frac{\rho_{\mathrm{WM}}\, S_{\mathrm{WM}} - \rho_{\mathrm{GM}}\, S_{\mathrm{GM}}}{\rho_{\mathrm{GM}}\, S_{\mathrm{WM}} + \rho_{\mathrm{GM}}\, S_{\mathrm{GM}}} \quad [15]$$

and:

$$\hat{c}^{(\rho)} = \frac{\rho_{\mathrm{WM}}\,\hat{S}_{\mathrm{WM}} - \rho_{\mathrm{GM}}\,\hat{S}_{\mathrm{GM}}}{\rho_{\mathrm{GM}}\,\hat{S}_{\mathrm{WM}} + \rho_{\mathrm{GM}}\,\hat{S}_{\mathrm{GM}}}\,, \qquad [16]$$

where the WM and GM signals and their corresponding nominal values are denoted by $S_{\mathrm{WM/GM}}$ and $\hat{S}_{\mathrm{WM/GM}}$.

Besides performance considerations, it is important also to test the robustness of the signal domain optimization which relies on a given choice for the T_1 interval I. An adverse effect would be for example that the optimization of $U_{f,\lambda}$ generates pulses with strongly degraded properties outside the interval I. Such a scenario can be tested by evaluating the standard deviation of the contrast map $c_s(\mathrm{T}_1, \mathrm{T}_1{}')$ in the following two cases: a) $\mathrm{T}_1/\mathrm{T}_1{}' = 1300/500$ ms and b) $\mathrm{T}_1/\mathrm{T}_1{}' = 1300/3000$ ms. These tests thus determine the contrast $c_{s,\mathrm{hyper}}$ between an hyper-intense region (case a) or an hypo-intense (case b) region and WM. The robustness of the signal domain optimization is thus assessed with the following metrics:

$$\sigma_{c,\mathrm{hypo/hyper}} = \frac{\mathrm{Var}\left(c_{s,\mathrm{hypo/hyper}}\right)^{1/2}}{c_{\hat{s},\mathrm{hypo/hyper}}}\,. \qquad [17]$$

The last theoretical aspect treated in this work concerns the analysis of the influence of the norm coefficient p on the pulse optimization results. We concentrate in particular on the tail of the distribution of the WM signal (S_{WM}) and the WM-GM contrast $c^{(\rho)}$ and analyze to which extent the L_3- and L_5-norms allow reducing the 5 % quantile of the distribution of S_{WM} and $c^{(\rho)}$.

Numerical field maps

The head model used for the RF field simulations is representative of an adult male head and was constructed from 1.5 T anatomical images, acquired with 1 mm isotropic resolution. Details on the construction of this model can be found in (19, 20). The RF simulations distinguish 10 types of tissue on the basis of the respective density, conductivity and relative permittivity values. The coil model represents a 12 channel pTx head coil designed in the laboratory. Full-wave simulations with the loaded coil were performed with HFSS (Ansys, Pittsburgh, PA, USA) for an operation at 297 MHz (7 T). The calculated electric and magnetic field distributions were then exported onto a Cartesian grid of 5 mm isotropic resolution.

In order to feed the twelve channels of the head coil with eight RF power amplifiers (transmitters), a singular value decomposition (SVD) of the matrix $B_1^+ = (B_{1,[n]}(r_m)^+)_{m,n} \in \mathbb{C}^{N_v \times 12}$ was performed (21). The eigenvectors corresponding to the eight largest singular values were then taken as an input basis. The simulated electric fields were then exploited to compute the Q-matrices averaged over 10 g contiguous tissue, on which the virtual observation point compression scheme (16) was applied with an overestimation parameter ϵ_G of 2 to reduce the number of local SAR constraints from 3.73×10^4 down to $\sim$200.

For the simulations to be more realistic, the static field offset ΔB_0 was also taken into account and was obtained by a first-order perturbation approach to Maxwell's equations (22) and by assuming the uniform magnetic field susceptibility of water over the whole model.First and second order spherical harmonics variations were removed by fitting, again to mimic typical experimental conditions.

k_T-points pulse design

The number of k_T-points was set to 5 for the SFA and 7 for the inversion pulse. Based on previous work (6, 10), their respective RF sub-pulse durations were 80 and 650 μs while the blip durations were 60 μs, which resulted in total pulse durations of 700 μs and 5 ms. For the inversion pulse, we used for the k_T-points placement a star-shaped trajectory centered at the origin of the k-space and with the six vertexes located at 4 m^{-1} from the center, so that the distance between k_T points roughly matches the wavelength of the electromagnetic field inside the brain, as recommended in (23). For the excitation pulse, a star-shaped trajectory, this time contained in the k_y-k_z plane, was used. For simplicity, the placement of the k_T points in k-space thus was not optimized. Intelligent placement or joint optimization methods could be used to yield more optimal solutions (24–26).

Search algorithm

The minimization of the objective functions U_α and $U_{f,\lambda}$ involves non-convex optimization problems. A convergence to the global optimum is thus not guaranteed, but a local optimum can still be satisfying, if the solution in question yields good performances. In Ref. (10), it was found that an initialization of the RF coefficients with the variable-exchange (VE)

method (9) yields a robust descent and that the returned performance was close to that of the global optimum. We thus tackled the minimization of U_α as follows:

Step 1 Solve the MLS problem separately for the inversion and the SFA pulses using the SFA approximation the VE method and with no constraint; denote by $\hat{\mathbf{x}}^{(\mathrm{VE})}$ and $\hat{\mathbf{y}}^{(\mathrm{VE})}$ the respective solutions;

Step 2 Solve the joint problem (Eq. 6) using the active-set (A-S) algorithm of Matlab (Mathworks, Natick, MA, USA) and the initial point $(\hat{\mathbf{x}}^{(\mathrm{VE})}, \hat{\mathbf{y}}^{(\mathrm{VE})})$ until convergence; denote by $(\hat{\mathbf{x}}^{(U_\alpha)}, \hat{\mathbf{y}}^{(U_\alpha)})$ the solution;

In Step 2, the A-S algorithm was provided with the constraints (1 constraint for the global SAR, 190 constraints for the 10 g local SAR, $(5+7)\times 8 = 96$ constraints for the peak power and 8 constraints for the average power) and the gradient of the constraints in analytic form (10). The gradient of the objective function, calculated by finite differences, was also provided. The alternative signal domain optimization problem was then solved by simply adding to the FA domain optimization the following step:

Step 3 Run the A-S algorithm on the new problem obtained from Eq. 6 by replacing the objective function U_α by $U_{f,\lambda}$ until convergence, and using $(\hat{\mathbf{x}}^{(U_\alpha)}, \hat{\mathbf{y}}^{(U_\alpha)})$ as initialization value; denote by $(\hat{\mathbf{x}}^{(U_f)}, \hat{\mathbf{y}}^{(U_f)})$ the solution.

In practice, for the signal domain optimization, Step 2 can be run with only a few A-S iterations without affecting the convergence in Step 3. It is recommended however to maintain this step in the case $\lambda = 0$ (i.e. without contrast term in the cost function) as there is a risk otherwise to converge towards another worse local minimum, characterized by an FA distribution for the SFA pulse on average greater than the Ernst angle. For the case of $\lambda > 0$, the approach seems more robust and Step 2 could be skipped.

To speed up the calculation, the objective function value and its derivatives were computed on a GPU device (Nvidia, Santa Clara, CA, Tesla K20c) with single (32 bit) precision, combined with two processors E5-2670 and 128 GB of RAM. With this implementation, an evaluation of the objective function U_α and its gradient with 12000 voxels took less than 80 ms of computation time, while returning the optimized pulses $(\hat{\mathbf{x}}^{(U_\alpha)}, \hat{\mathbf{y}}^{(U_\alpha)})$ required less

than 30 s. The additional computation time for obtaining $(\hat{\mathbf{x}}^{(U_f)}, \hat{\mathbf{y}}^{(U_f)})$ was of the order of 40 to 80 s depending on the choice of λ and J.

L-curve construction

The L-curves were constructed for the objective functions U_α and $U_{f,\lambda}$ with $\lambda = 0$, 1, 2 and 5 and, for each value of λ, with $J = J_1 \equiv (\mathrm{T_{1WM}}, \mathrm{T_{1GM}})$ and $J \equiv J_2$ composed of 4 $\mathrm{T_1}$ values distributed evenly in the interval $[\mathrm{T_{1WM}} - 200\,\mathrm{ms}, \mathrm{T_{1GM}} + 200\,\mathrm{ms}]$, where $\mathrm{T_1}$ values of 1.3 and 2 s were assumed for WM and GM respectively (17). The maximum local SAR value considered in the simulation was 10 W/kg, which corresponds to the limit recommended by the IEC for a head scan (27). Additionally, three norms were used for computing the L-curves: L_2, L_3 and L_5-norms. For computing the objective function $U_{f,\lambda}$, the following parameters were used for the MPRAGE pulse sequence: TR/TI/ES/TE = 2600/1100/6.5/3 ms and nominal FA = 9°. The inversion pulse naturally targeted 180° throughout.

Experimental validation in vivo

The RF pulse design strategies were applied to human brain imaging on a 7 T Magnetom Scanner (Siemens Healthcare, Erlangen, Germany) equipped with an 8 channel transmit array (1 kW peak power per channel) and an AC84 head gradient system (50 mT/m maximum amplitude and 333 T/m/s maximum slew rate). Sequence parameters for the MPRAGE were chosen consistently with the simulation parameters. Other parameters were readout bandwidth of 240 Hz, ETL = 160, 1 mm isotropic resolution with a $256 \times 208 \times 160$ matrix in sagittal acquisition and a total acquisition time (TA) of 9 min. For the pulse optimization, the peak and average power limits were set at the coil input to 450 W and 8 W per channel respectively. The global SAR limit was set to 3.2 W/kg (27). The RF sub-pulse durations, blip durations and number of k_T-points were identical to those used in the simulations. With these settings, three RF pulse designs were performed, according to the following criteria and local SAR limits i) minimization of U_α with 3 W/kg ii) $U_{f,\lambda}$ with 3 W/kg and iii) U_α with 6 W/kg. The study was approved by our institutional review board. Measurements were performed on five adult volunteers who provided informed consent.

The MPRAGE protocol was applied following a preparation protocol dedicated to the characterization of the ΔB_0 and B_1 field distributions. This protocol was composed of a 3D multiple echo gradient echo (GRE) (2.5 mm isotropic resolution, matrix size $128 \times 96 \times 64$, TR = 25 ms, TE = 5/6.5/8 ms) for estimating the static field offset, and a multi-slice interferometric XFL acquisition (28–30) (5 mm resolution) for estimating the 8 complex transmit B_1 fields in 3D for each channel. The 3D GRE served also for computing the brain mask using FSL BET (31).

In previous examinations, an MPRAGE image of the same volunteers was also acquired at 3 T on a Magnetom Tim Trio (Siemens Healthcare, Erlangen, Germany) equipped with a whole body transmit RF coil and a 32-channel receive head coil. The sequence parameters were TI = 900 ms, TR = 2300 ms, TE = 3 ms, FA = 9°, readout bandwidth of 240 Hz, ETL = 160, $1 \times 1 \times 1.1$ mm resolution with a $256 \times 240 \times 160$ matrix in sagittal acquisition and TA = 7.8 min.

The obtained MPRAGE images were analyzed with SPM12 for simultaneous bias field correction and segmentation (32), and for realignment of the different acquisitions.

SAR management

The entire MRI protocol at 7 T was applied under real-time local SAR monitoring (Tim Tx Array Step 2) which, in accordance with internal regulations, was based on two collections of VOPs, a male (the same model as the one used in the simulation study) and a female subject, pooled together. To account for additional anatomical variability, an overestimation factor of 1.4 was included (33). An error propagation factor was also included in the Q-matrix calculation to account for uncertainties in the coil model (34), created in HFSS, which increases the SAR by roughly a factor of 1.25. Finally, an overestimation factor of 1.55 was applied to overcome measurement errors in the scanner's monitoring hardware (35), thus yielding a total overestimation factor of $\simeq 2.8$ compared to the raw SAR. By taking the phase of the RF waveforms into account, this security margin for the moment appears necessary to ensure patient safety; yet it remains by far less conservative than other approaches where only the amplitude or average power is used in SAR calculations (15, 36).

Prior to each measurement in vivo, a test sequence was run on a phantom under local

SAR management in order to verify that the maximum local SAR calculated by the scanner's monitor, based on the measured RF waveforms, matched the theoretical value, based on the ideal RF pulse shapes. The results, shown in Fig. 2, provide a last verification of the consistency between the VOPs used for RF pulse design and the ones used for real-time monitoring, thereby preventing the scanner from stopping unnecessarily and reinforcing patient safety.

Results

L-curve simulations

The L-curve simulation results obtained for the L_2 norm are displayed in Fig. 3 for the objective functions U_α and $U_{f,\lambda}$ for two choices of J ($J = J_1$, 2 T_1 values, and $J = J_2$, 4 T_1 values), and for 3 values of λ ($\lambda = 0, 2, 5$). This result shows that the objective function $U_{f,\lambda}$ often outperforms U_α not only with regards to the metrics $f_{s,\mathrm{RMS}}$ and $f_{c,\mathrm{RMS}}$ (Figures 3a-b), but also in terms of the WM signal, the GM signal and the WM-GM contrast standard deviations (Figs. 3c-e). It also appears that the number of T_1 values (J_1 versus J_2) used for computing $U_{f,\lambda}$ influences only moderately the result of the optimization. Since in practice, using large sets is computationally demanding, we therefore recommend to use the minimal set $J_1 = (T_{1\mathrm{WM}}, T_{1\mathrm{GM}})$ for the definition of $U_{f,\lambda}$. Regarding the influence of the weighting factor λ, as expected, the case $\lambda = 0$ is clearly optimal with regard to the signal fidelity but gives slightly poorer contrast fidelity than U_α. Now, taking $\lambda \geq 2$ improves the contrast fidelity but degrades slightly the signal fidelity. Furthermore, taking $\lambda = 5$ leads only to a very small contrast improvement compared to the case $\lambda = 2$, so that the latter weighting appears to us roughly as the best choice.

The elbow of the L-curves associated with the objective function U_α, i.e. the point where the curvature of the L-curve is maximized, is reached for $2 \leq \mathrm{SAR}_{10\mathrm{g,max}} \leq 3$ W/kg. Under the constraint $\mathrm{SAR}_{10\mathrm{g,max}} \leq 3$ W/kg, we have at the optimum of U_α: $\sigma_{\mathrm{WM}} = 11$ %, $\sigma_{\mathrm{GM}} = 24$ % and $\sigma_{c^{(\rho)}} = 13\%$ whereas we obtain the values 6 %, 13 % and 14 % with the minimization of $U_{f,0}$ and 7 %, 14 % and 11 % with $U_{f,2}$. To illustrate the associated difference

in MR images, the MPRAGE signal was simulated using simplified T_1 and PD distributions (T_1 = 1.3/1.8/2/4 s and PD = 0.7/0.75/0.8/1 respectively for WM, cerebellum, cortical GM and CSF) and the actual FA distributions returned by the different optimizations. A comparison is provided in Fig. 4 for different slices and orientations and shows qualitatively the importance of the contrast fidelity and thus the superiority of the objective $U_{f,2}$ over $U_{f,0}$.

In Table 1, the five metrics used for the construction of the L-curves but also the FA standard deviation as well as the standard deviation of the contrast maps for a hyper-signal and a hypo-signal are reported for the three settings discussed above.

The influence of the norm (L_2, L_3 or L_5) on image quality is shown in Table 2 where the standard deviation and 5 %-quantile are reported for the WM signal the WM-GM contrast. Interestingly, for the function U_α, the L_3 norm is successful in reducing both the standard deviations and the 5 %-quantiles while this does not apply for $U_{f,\lambda}$.

In vivo results

The MPRAGE images obtained in one of the volunteers are shown in Fig. 5, after bias field correction. The first row corresponds to the 3 T MPRAGE image whereas rows 2-4 show the MPRAGE images obtained at 7 T with the various RF pulse optimization strategies (objective function and local SAR limit): i) U_α and 3 W/kg (row 2), ii) $U_{f,2}$ and 3 W/kg (the proposed approach, row 3), and iii) U_α and 6 W/kg (row 4). Increasing the local SAR limit to 6 W/kg (row 4) allows recovering many regions but to the expense of a higher SAR deposition. The four boxes in Fig. 5, magnified in Fig. 6 for rows 2 and 3, indicate regions in the brain where the WM-GM contrast is enhanced with the proposed RF pulse design in comparison with the standard FA optimization.

To verify that the improvements shown in Fig. 5 have globally a positive impact on the WM-GM contrast and on image segmentation, we evaluated for each subject and for each MPRAGE acquisition i) the similarity between the segmentation of the brain at 3 T and at 7 T and ii) the separation of the WM and GM signal distributions. The similarity between the 3 T and 7 T segmentations was defined as the number of voxel with identical classification divided by the total number of voxels, whereby the classification was obtained by taking the

tissue type displaying the highest probability. The separation was defined as the quantity $(S_{\mathrm{WM}} - S_{\mathrm{GM}})/(S_{\mathrm{WM}} + S_{\mathrm{GM}})$ where S_{WM} and S_{GM} represent the modes of the histograms for the WM and GM signals respectively, calculated from the signal distributions at 7 T observed within the 3 T WM and GM masks. The results of this analysis are presented as bar plots in Fig. 7. In all cases, the similarity with the 3 T segmentation and the global WM-GM contrast signal was slightly improved by using the signal domain optimization.

Discussion

The RF pulse design simulations have shown that under identical power and SAR constraints, the signal domain optimization (objective function $U_{f,\lambda}$) improved significantly the WM signal, the GM signal and the WM-GM contrast homogeneity compared to the FA domain optimization (7). In the proposed optimization, the presence of the contrast term F_c was important furthermore to drive the optimization to a solution with a better contrast fidelity than the FA domain optimization, while guaranteeing also higher signal uniformity. In the FA domain optimization, given that the homogeneity of the excitation and inversion profiles have different impacts on the signal and contrast homogeneity, introducing different weights for the inversion pulses relatively to the SFA pulse could yield better pulse performance than taking equal weights, as imposed by Eq. 6. However, this refinement would not exploit the *interplay* between the SFA and the inversion pulse to optimize the signal and contrast fidelity. The performance metrics reported in Table 1 also indicate that the contrast for a hyper- or a hypo-intense region in the MPRAGE image is not degraded by minimizing $U_{f,\lambda}$, although the T_1 values assumed for the hyper- and hypo-intensity (e.g. characteristic of the presence of an edema or a tumor) lie outside the interval I used in the definition of f_s and f_c. In Table 1, it can also be seen that the FA deviation is in fact increased at the optimum of $U_{f,0}$ or $U_{f,2}$ compared to U_α. However, this result is not in contradiction with an improvement of the other metrics and only reflects the fact that the SFA and inversion pulses are optimized in the signal domain rather than in the FA domain.

The potential of the L_p norm with $p > 2$ to further improve RF pulse performance has also been shown with the L_3 norm applied to U_α, with a reduction of the 5 % quantile and

the standard deviation of the WM signal and the WM-GM contrast, but still with a lower performance than for $U_{f,2}$ and the norm L_2. Surprisingly, increasing further p to 5 did not reduce further the 5 % quantile. Hence, the norm coefficient was kept equal to the standard value $p = 2$ for the in vivo validation. Larger p values normally tend to penalize further large errors, but also increases sensitivity to experimental errors and outliers.

The FA domain and the signal-domain optimization metrics were implemented in the MPRAGE acquisition in vivo whereby a comparison was performed between both RF pulse design strategies under identical SAR constraints, namely $\mathrm{SAR}_{10g} \leq 3$ W/kg. Direct visual inspection of the MPRAGE images confirms that the optimization of the signal and contrast homogeneity improves image quality. The improvement was most obvious in the occipital lobe where a signal drop (in Fig. 5, second row, axial and coronal view) was suppressed. A clear enhancement was also seen in the temporal lobes with a significant reduction of the hyper-signal in the vicinity of the ear canal. Such a hyper-signal is most likely caused by an incomplete inversion of the magnetization which results in a signal increase and a severe loss of contrast. The second and third MPRAGE acquisitions (i.e., third and fourth row in Fig. 5) indicate on the other hand that the RF pulse design performed in the FA domain with the less stringent local SAR limit $\mathrm{SAR}_{10g} \leq 6$ W/kg does not seem to provide a better image quality than the signal domain optimization with 3 W/kg local SAR limit. Thus we verified that the proposed new RF pulse design allows for a significant reduction of the local SAR while maintaining homogeneous signal and contrast, leaving room for a possible additional safety factor without image degradation.

Conclusion

In this work, an alternative RF pulse design for the MPRAGE sequence has been developed which uses the signal as a surrogate of the FA in the optimization of the RF pulses. The method exploits the possibilities of a joint optimization of the SFA and inversion pulses and takes into account the non-linear dependence of the MPRAGE signal with the FAs. The results obtained show two possible applications of the method: an improvement in image quality or a significant reduction of the SAR at equivalent image quality. Our investigation

targeted exclusively the MPRAGE sequence but since many sequences exhibit a non-linear signal dependence with the FA, it unveils a possible direction for further improvements in other sequences.

Acknowledgements

The research leading to these results has received funding from the European Research Council under the European Union's Seventh Framework Program (FP7/2013-2018) / ERC Grant Agreement n. 309674.

List of Figures

Figure 1 Maps of a) the FA deviation $f_\alpha = \left(\left(\frac{\alpha_{\mathrm{Inv}}}{\alpha_{\mathrm{t,Inv}}} - 1 \right)^2 + \left(\frac{\alpha_{\mathrm{SFA}}}{\alpha_{\mathrm{t,SFA}}} - 1 \right)^2 \right)^{1/2}$ as used in Eq. 6, b) the signal fidelity f_s (Eq. 7), c) the contrast fidelity f_c (Eq. 9) and c) the mixed fidelity map $(f_s^2 + f_c^2)^{1/2}$ as a function of α_{Inv} (**x**-axis) and α_{SFA} (**y**-axis). These are computed for $p = 2$ and for the following MPRAGE sequence parameters: TR/TI/ES/TE = 2600/1100/6.5/3 ms, nominal FA 180°/9° respectively for the inversion and FLASH pulses. There is an interplay between the two different angles for f_s^2 and f_c^2, in the sense that they are not additively separable in α_{SFA} and α_{Inv}. The FA deviation on the other hand is the sum of two quadratic terms in the α_{SFA} and α_{Inv} directions.

Figure 2 Comparison of the local SAR calculation performed by the scanner's SAR monitor (based on the RF waveforms measured in real time via directional couplers) for each VOP with the theoretical calculation (based on ideal RF pulse shapes). Both calculations include the same local SAR overestimation factor ($\simeq 2.8$), the latter being included in the Q-matrix of each VOP.

Figure 3 L-curve simulations at 7 T showing the trade-off between local SAR and a) signal fidelity b) contrast fidelity c) WM signal standard deviation d) GM signal standard deviation and e) WM-GM contrast standard deviation for different pulse optimization methods: U_α (blue), $U_{f,\lambda}$ with $\lambda = 0$ (red), $\lambda = 2$ (black) and $\lambda = 5$ (green). For the objective function $U_{f,\lambda}$, two sets of T_1 values were taken: $J = J_1$, i.e. two T_1 values (solid line) and $J = J_2$, i.e. four T_1 values (dashed lines). This analysis shows in particular that the number of T_1 values (J_1 versus J_2) used to probe the T_1 interval does not have a strong impact.

Figure 4 Simulated 7 T MPRAGE images of the head obtained with the nominal excitation (9° and 180°), and with the minimization of the objective functions U_α (second row), $U_{f,0}$ (third row) and $U_{f,2}$ (fourth row) and with a local SAR limit of 3 W/kg. The latter two objective functions yield better fidelity to the reference image than the FA optimization. The red arrows also indicate two locations where adding the contrast term in the signal domain optimization (third row) allows for a better preservation of the WM-GM contrast than without (second row). In these simulations, simplified PD and T_1 distributions were assumed with 4 different values for WM, cortical GM, cerebellum and CSF.

Figure 5 MPRAGE images of the brain obtained in one healthy volunteer in sagittal, axial and coronal orientation (2 slices for each orientation). The first row represents the 3 T MPRAGE acquisition. Rows 2 to 4 correspond to the 7 T acquisitions under the following conditions: i) $\mathrm{SAR}_{10g} \leq 3$ W/kg and minimization of U_α (row 2), ii) $\mathrm{SAR}_{10g} \leq 3$ W/kg and minimization of $U_{f,2}$ (row 3) and iii) $\mathrm{SAR}_{10g} \leq 6$ W/kg and minimization of U_α (row 4). The red arrows indicate regions where strong artifacts occur (contrast loss, signal loss or hyper-signals) in i) due to residual transmit B_1 inhomogeneities, which are removed, or at least reduced in ii). The boxes indicate four regions which are zoomed in a subsequent figure to highlight some differences between both pulse designs under the local SAR constraint of 3 W/kg. A slight artifact, visible in the sagittal views, is caused by the strong non-linearity of the head gradient outside the FOV. As a consequence, signal residuals coming from the shoulders in particular can appear in the reconstructed image.

Figure 6 Zooms of the second and third row of Fig. 5, emphasizing the improvement obtained with direct optimization of the MPRAGE signal (images a'-d') compared to the standard FA optimization (images a-d) under the local SAR constraint of 3 W/kg.

Figure 7 Bar plots of a) the WM-GM peak separation and b) the similarity with the 3 T segmentation for the 3 MPRAGE acquisitions in vivo at 7 T.

List of Tables

Table 1 Simulated performance of the three pulse design strategies (objective functions U_α, $U_{f,0}$ and $U_{f,2}$) under the local SAR constraint $\mathrm{SAR}_{10\mathrm{g,max}} = 3$ W/kg. The first five metrics are those used for the L-curves. The standard deviation of the hyper-signal $\sigma_{c,\mathrm{hyper}}$ and the hypo-signal $\sigma_{c,\mathrm{hypo}}$ contrast maps are reported as well as the FA NRMSEs $< (\alpha_{\mathrm{SFA}}/\alpha_{\mathrm{t,SFA}} - 1)^2 >^{1/2}$ and $< (\alpha_{\mathrm{Inv}}/\alpha_{\mathrm{t,Inv}} - 1)^2 >^{1/2}$. All values are given in percentage.

Table 2 Influence of the norm's coefficient p on the WM signal and the WM-GM contrast statistics for the 7 T RF pulse design simulations. All values are given in percentage.

References

[1] Mugler JP, Brookeman JR. Three-dimensional magnetization-prepared rapid gradient-echo imaging (3d MP RAGE). Magn Reson Med 1990;15:152–157.

[2] Deichmann R, Good CD, Josephs O, Ashburner J, Turner R. Optimization of 3-D MP-RAGE Sequences for Structural Brain Imaging. NeuroImage 2000;12:112–127.

[3] Han X, Jovicich J, Salat D, Kouwe Avd, Quinn B, Czanner S, Busa E, Pacheco J, Albert M, Killiany R, Maguire P, Rosas D, Makris N, Dale A, Dickerson B, Fischl B. Reliability of MRI-derived measurements of human cerebral cortical thickness: The effects of field strength, scanner upgrade and manufacturer. NeuroImage 2006;32:180–194.

[4] Bernstein MA, Huston J, Ward HA. Imaging artifacts at 3.0T. Journal of Magnetic Resonance Imaging 2006;24:735–746.

[5] Katscher U, Börnert P, Leussler C, van den Brink JS. Transmit SENSE. Magn Reson Med 2003;49:144–150.

[6] Cloos MA, Boulant N, Luong M, Ferrand G, Giacomini E, Le Bihan D, Amadon A. kT-points: Short three-dimensional tailored RF pulses for flip-angle homogenization over an extended volume. Magn Reson Med 2012;67:72–80.

[7] Cloos MA, Boulant N, Luong M, Ferrand G, Giacomini E, Hang MF, Wiggins CJ, Bihan DL, Amadon A. Parallel-transmission-enabled magnetization-prepared rapid gradient-echo T1-weighted imaging of the human brain at 7T. NeuroImage 2012;62:2140–2150.

[8] Cloos MA, Boulant N, Luong M, Ferrand G, Giacomini E, Hang MF, Wiggins CJ, Le Bihan D, Amadon A. kT-points based inversion pulse design for transmit-sense enabled MP-RAGE brain imaging at 7 T. In Proceedings of the 20th Annual Meeting of ISMRM. Melbourne, Australia 2012; p. 634.

[9] Setsompop K, Wald L, Alagappan V, Gagoski B, Adalsteinsson E. Magnitude least squares optimization for parallel radio frequency excitation design demonstrated at 7 Tesla with eight channels. Magn Reson Med 2008;59:908–915.

[10] Hoyos-Idrobo A, Weiss P, Massire A, Amadon A, Boulant N. On Variant Strategies to Solve the Magnitude Least Squares Optimization Problem in Parallel Transmission Pulse Design and Under Strict SAR and Power Constraints. IEEE Transactions on Medical Imaging 2014;33:739–748.

[11] Guérin B, Gebhardt M, Cauley S, Adalsteinsson E, Wald LL. Local specific absorption rate (SAR), global SAR, transmitter power, and excitation accuracy trade-offs in low flip-angle parallel transmit pulse design. Magn Reson Med 2014;71:1446–1457.

[12] Boulant N, Hoult DI. High tip angle approximation based on a modified Bloch–Riccati equation. Magn Reson Med 2012;67:339–343.

[13] Grissom W, Yip Cy, Zhang Z, Stenger VA, Fessler JA, Noll DC. Spatial domain method for the design of RF pulses in multicoil parallel excitation. Magn Reson Med 2006; 56:620–629.

[14] Eichfelder G, Gebhardt M. Local specific absorption rate control for parallel transmission by virtual observation points. Magn Reson Med 2011;66:1468–1476.

[15] Graesslin I, Homann H, Biederer S, Börnert P, Nehrke K, Vernickel P, Mens G, Harvey P, Katscher U. A specific absorption rate prediction concept for parallel transmission MR. Magn Reson Med 2012;68:1664–1674.

[16] Lee J, Gebhardt M, Wald LL, Adalsteinsson E. Local SAR in parallel transmission pulse design. Magn Reson Med 2012;67:1566–1578.

[17] Rooney WD, Johnson G, Li X, Cohen ER, Kim SG, Ugurbil K, Springer CS. Magnetic field and tissue dependencies of human brain longitudinal 1h2o relaxation in vivo. Magn Reson Med 2007;57:308–318.

[18] Bell BA, Smith MA, Kean DM, McGhee CN, MacDonald HL, Miller JD, Barnett GH, Tocher JL, Douglas RH, Best JJ. Brain water measured by magnetic resonance imaging. Correlation with direct estimation and changes after mannitol and dexamethasone. Lancet 1987;1:66–69.

[19] Massire A, Cloos MA, Luong M, Amadon A, Vignaud A, Wiggins CJ, Boulant N. Thermal simulations in the human head for high field MRI using parallel transmission. Journal of Magnetic Resonance Imaging 2012;35:1312–1321.

[20] Makris N, Angelone L, Tulloch S, Sorg S, Kaiser J, Kennedy D, Bonmassar G. MRI-based anatomical model of the human head for specific absorption rate mapping. Medical & Biological Engineering & Computing 2008;46:1239–1251.

[21] Ferrand G, Luong M, Cloos MA, France A, Amadon A, Boulant N, Darrasse L. SVD-based Hardware Concept to Drive N Transmit Elements of a Phased Array Coil with M <= N channels for High Field MRI. In Proceedings of the 19th Annual Meeting of ISMRM 2011; Abstract 3633.

[22] Salomir R, de Senneville BD, Moonen CT. A fast calculation method for magnetic field inhomogeneity due to an arbitrary distribution of bulk susceptibility. Concepts in Magnetic Resonance Part B: Magnetic Resonance Engineering 2003;19B:26–34.

[23] Amadon A, Dupas L, Vignaud A, Boulant N. Does the best distance beween 2 spokes match the inverse RF wavelength ? In Proceedings of the 23rd Annual Meeting of ISMRM. Toronto, Ontario, Canada 2015; p. 2388.

[24] Zelinski AC, Wald LL, Setsompop K, Alagappan V, Gagoski BA, Goyal VK, Adalsteinsson E. Fast slice-selective radio-frequency excitation pulses for mitigating B1+ inhomogeneity in the human brain at 7 Tesla. Magn Reson Med 2008;59:1355–1364.

[25] Ma C, Xu D, King KF, Liang ZP. Joint design of spoke trajectories and RF pulses for parallel excitation. Magn Reson Med 2011;65:973–985.

[26] Grissom WA, Khalighi MM, Sacolick LI, Rutt BK, Vogel MW. Small-tip-angle spokes pulse design using interleaved greedy and local optimization methods. Magn Reson Med 2012;68:1553–1562.

[27] Medical electrical equipment-part 2–33: particular requirements for the basic safety and essential performance of magnetic resonance equipment for medical diagnosis. 3rd ed Geneva: International Electrotechnical Commission 2010;603:2–33.

[28] Amadon A, Cloos MA, Boulant N, Hang MF, Wiggins CJ, Fautz HP. Validation of a very fast B1-mapping sequence for parallel transmission on a human brain at 7T. In Proceedings of the 20th Annual Meeting of ISMRM. Melbourne, Australia 2012; p. 3358.

[29] Fautz HP, Vogel M, Gross P, Kerr A, Zhu Y. B1 mapping of coil arrays for parallel transmission. In Proceedings of the 16th Annual Meeting of ISMRM. Toronto, Ontario, Canada 2008; p. 1247.

[30] Brunner DO, Pruessmann KP. B1+ interferometry for the calibration of RF transmitter arrays. Magn Reson Med 2009;61:1480–1488.

[31] Smith SM. Fast robust automated brain extraction. Human Brain Mapping 2002; 17:143–155.

[32] Ashburner J, Friston KJ. Unified segmentation. NeuroImage 2005;26:839–851.

[33] de Greef M, Ipek O, Raaijmakers AJE, Crezee J, van den Berg CAT. Specific absorption rate intersubject variability in 7T parallel transmit MRI of the head. Magn Reson Med 2013;69:1476–1485.

[34] Ferrand G, Luong M, Amadon A, Boulant N. Mathematical Tools to Define SAR Margins for Phased Array Coil In-Vivo Applications Given E-field Uncertainties. In Proceedings of the 23rd Annual Meeting of ISMRM. Toronto, Ontario, Canada 2015; p. 1862.

[35] Gumbrecht R. Development of customized pTx MR excitation methods and their safe application. Ph.D. thesis, Friedrich-Alexander-Universität Erlangen-Nürnberg, Erlangen 2013.

[36] Boulant N, Cloos MA, Luong M, Ferrand G, Wiggins CJ, Amadon A. Method for monitoring safety in parallel transmission systems based on channel-dependent average powers. In Proceedings of the 19th Annual Meeting of ISMRM. Montréal, Quebec, Canada 2011; Abstract 3504.

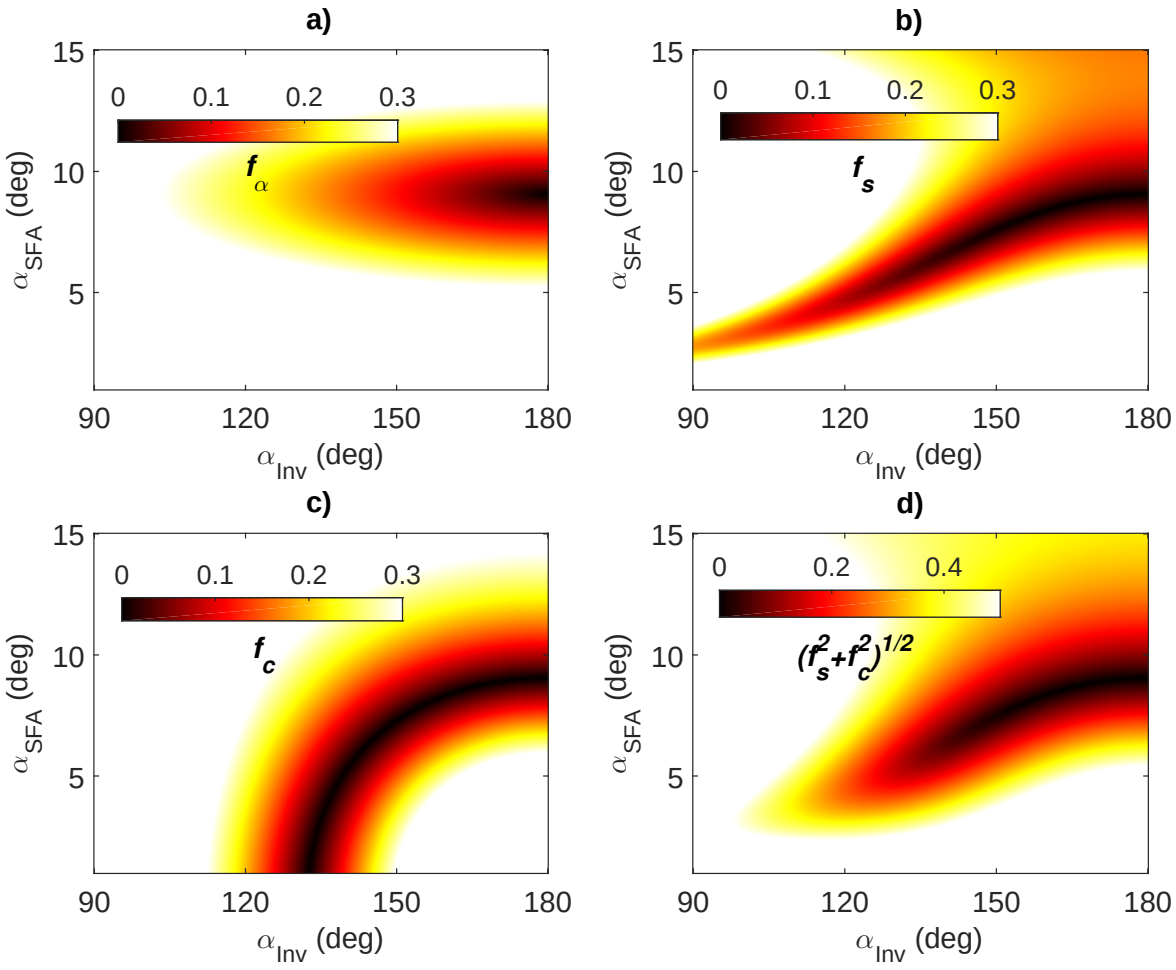
a)
b)
c)
d)
0
0.1
0.2
0.3
0.4
f_α
f_s
f_c
$(f_s^2+f_c^2)^{1/2}$
15
10
5
90
120
150
180
α_{SFA} (deg)
α_{Inv} (deg)

Figure 1

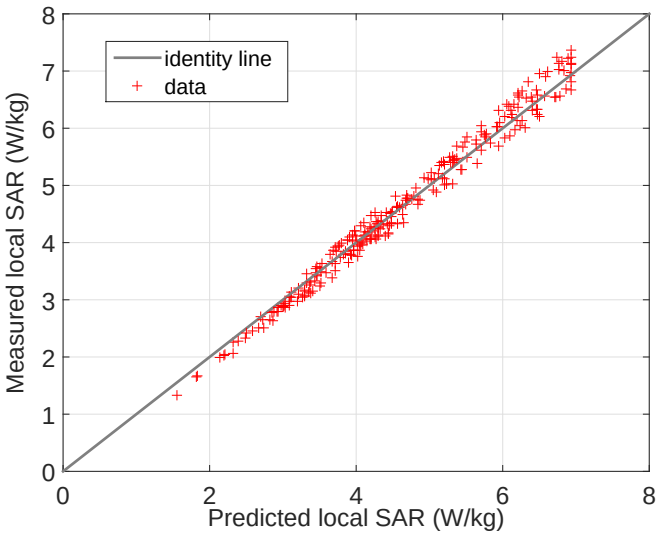
identity line
data
Measured local SAR (W/kg)
Predicted local SAR (W/kg)
0
1
2
3
4
5
6
7
8
0
2
4
6
8

Figure 2

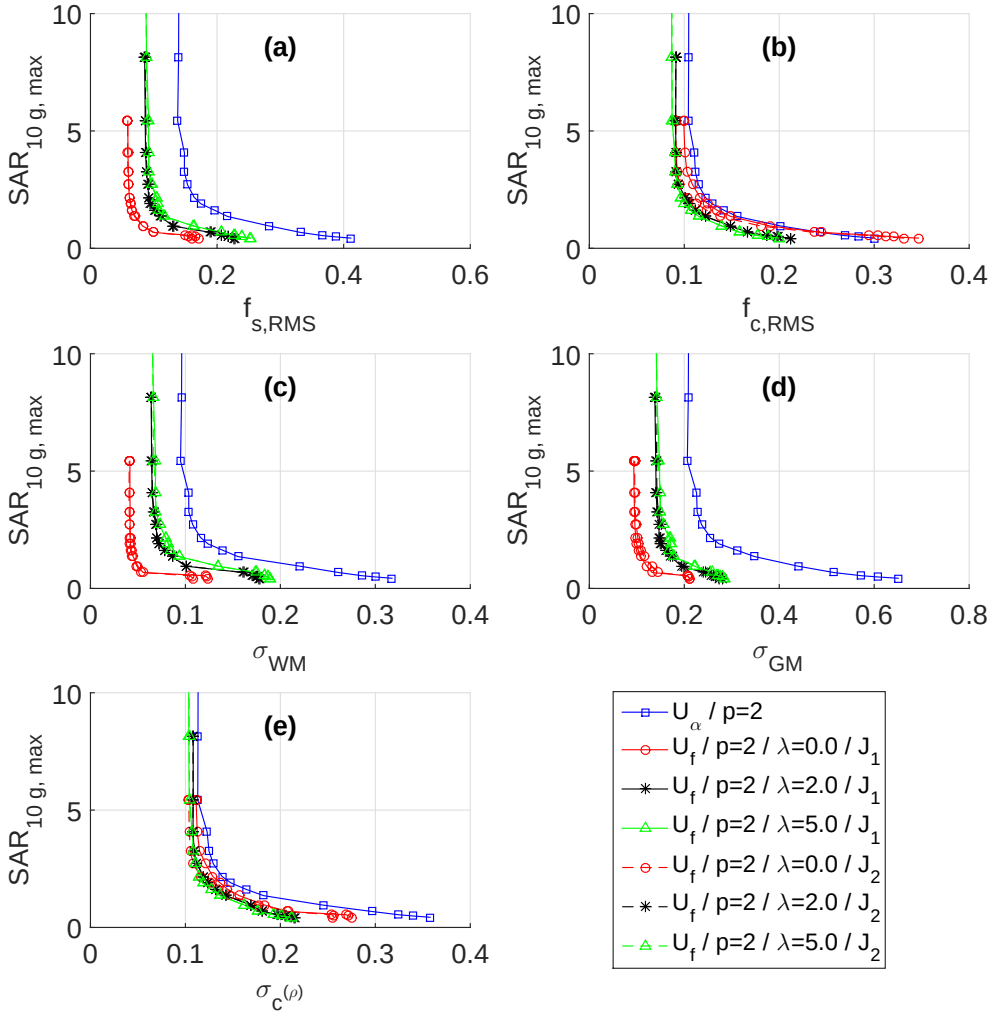
(a)
(b)
(c)
(d)
(e)
SAR10 g, max
fs,RMS
fc,RMS
σWM
σGM
σc(ρ)
Uα / p=2
Uf / p=2 / λ=0.0 / J1
Uf / p=2 / λ=2.0 / J1
Uf / p=2 / λ=5.0 / J1
Uf / p=2 / λ=0.0 / J2
Uf / p=2 / λ=2.0 / J2
Uf / p=2 / λ=5.0 / J2

Figure 3

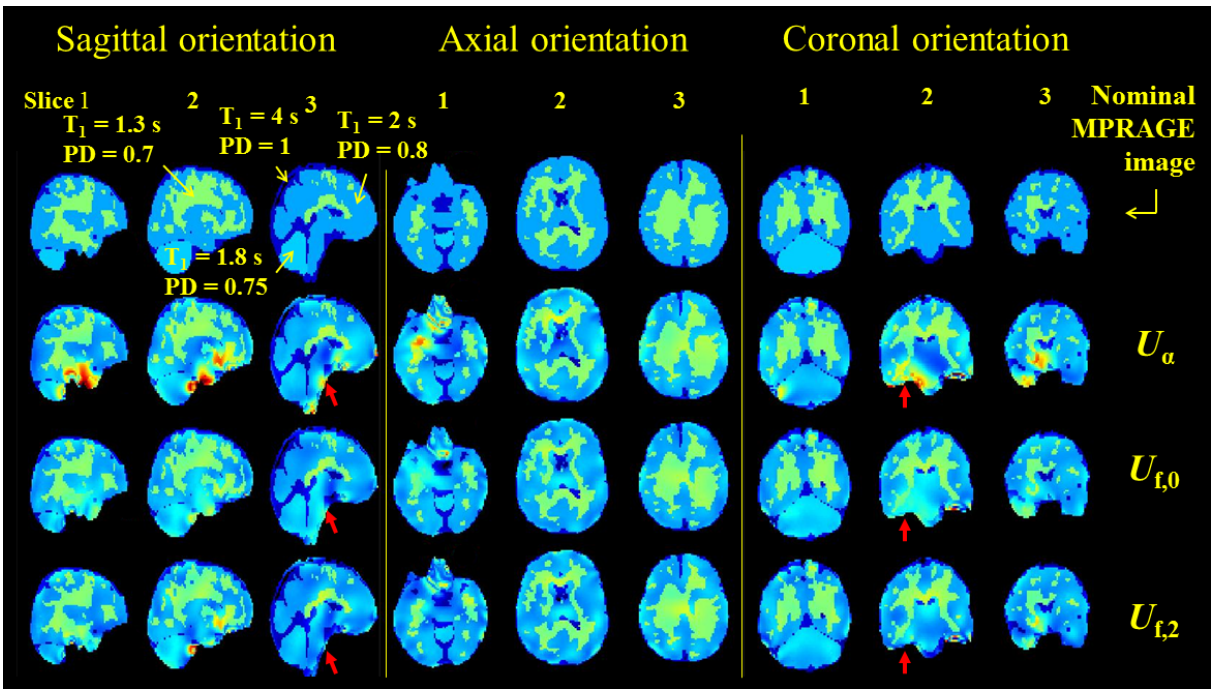
Sagittal orientation
Axial orientation
Coronal orientation
Slice 1
2
3
1
2
3
1
2
3
Nominal MPRAGE image
T1 = 1.3 s
PD = 0.7
T1 = 4 s
PD = 1
T1 = 2 s
PD = 0.8
T1 = 1.8 s
PD = 0.75
Uα
Uf,0
Uf,2

Figure 4

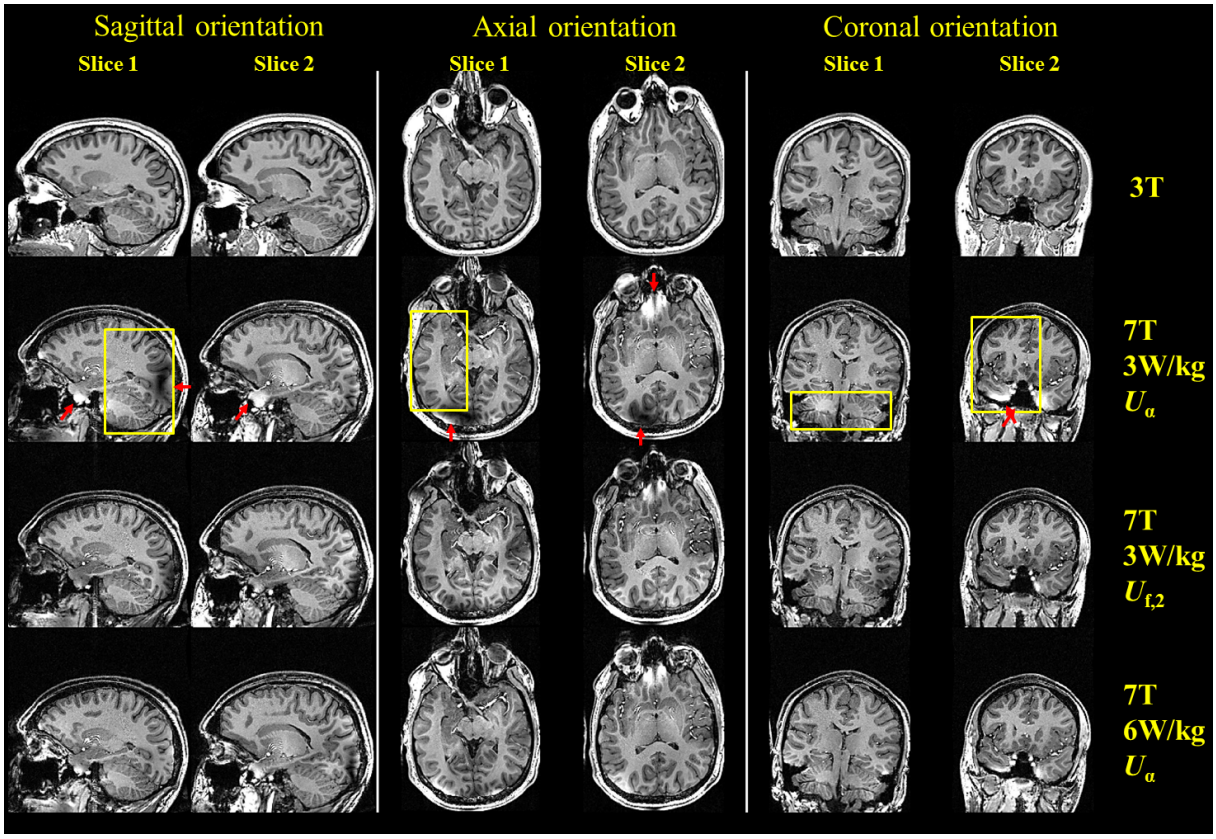
Sagittal orientation
Slice 1
Slice 2
Axial orientation
Slice 1
Slice 2
Coronal orientation
Slice 1
Slice 2
3T
7T
3W/kg
U_α
7T
3W/kg
$U_{f,2}$
7T
6W/kg
U_α

Figure 5

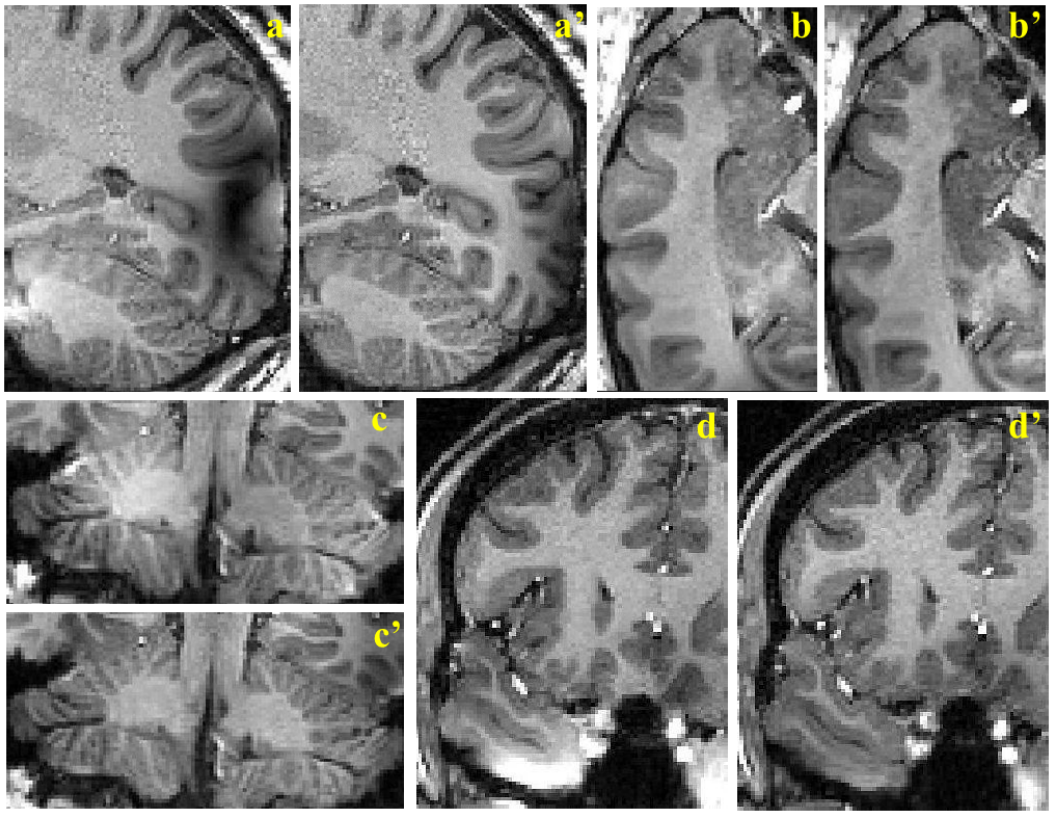

Figure 6

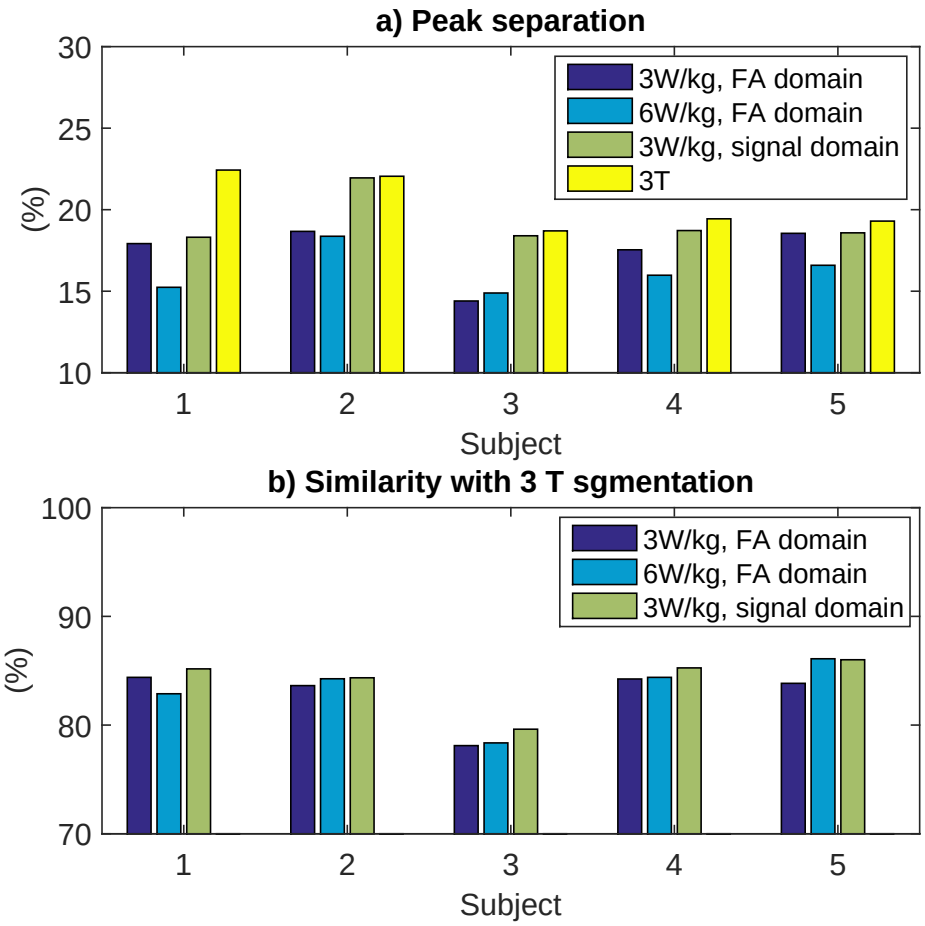
a) Peak separation
30
25
20
15
10
(%)
1
2
3
4
5
Subject
3W/kg, FA domain
6W/kg, FA domain
3W/kg, signal domain
3T
b) Similarity with 3 T sgmentation
100
90
80
70
(%)
1
2
3
4
5
Subject
3W/kg, FA domain
6W/kg, FA domain
3W/kg, signal domain

Figure 7

	U_α	$U_{f,0}$	$U_{f,2}$
$f_{s,\mathrm{RMS}}$	14.8	6.0	8.8
$f_{c,\mathrm{RMS}}$	11.2	10.3	9.2
σ_{WM}	10.4	4.2	6.6
σ_{GM}	22.7	9.5	14.3
$\sigma_{c^{(\rho)}}$	12.5	11.5	10.9
$\sigma_{c,\mathrm{hyper}}$	6.9	7.5	6.3
$\sigma_{c,\mathrm{hypo}}$	10.0	9.1	8.8
α_{Inv} NRMSE	13.2	17.8	15.8
α_{SFA} NRMSE	7.0	21.0	16.0

Table 1

	U_α			$U_{f,2}$		
	L_2	L_3	L_5	L_2	L_3	L_5
$\sigma_{S_{\mathrm{WM}}}$	10.4	9.5	8.9	6.6	6.8	9.0
$\sigma_{c^{(\rho)}}$	12.5	12.1	12.2	10.9	11.0	14.1
$Q_{S_{\mathrm{WM}}}(5\%)$	20.2	18.3	21.6	12.2	13.5	17.9
$Q_{c^{(\rho)}}(5\%)$	30.9	29.2	32.1	22.4	23.6	28.9

Table 2